Arabian Journal of Chemistry (2019) **12**, 1277–1289

King Saud University

Arabian Journal of Chemistry

www.ksu.edu.sa
www.sciencedirect.com

ORIGINAL ARTICLE

Stearate as a green corrosion inhibitor of magnesium alloy ZE41 in sulfate medium

Nandini Dindodi, A. Nityananda Shetty *

Department of Chemistry, National Institute of Technology Karnataka, Surathkal, Post Srinivasnagar, Mangalore 575025, Karnataka, India

Received 26 June 2013; accepted 5 November 2014
Available online 20 November 2014

KEYWORDS

Alloy;
Magnesium;
Impedance;
Polarization;
Stearate

Abstract The efficiency of stearate as a corrosion inhibitor for magnesium alloy ZE41 has been studied in sodium sulfate medium, employing electrochemical techniques like potentiodynamic polarization and electrochemical impedance spectroscopy (EIS). The results of polarization study imply that stearate functions as a mixed-type corrosion inhibitor with a predominant anodic control. The adsorption of stearate on alloy surface is found to obey the Langmuir adsorption isotherm. The proposed inhibition mechanism involved adsorption of stearate onto metal surface, followed by precipitation of magnesium stearate within the microdefects of $Mg(OH)_2$ surface film which enhanced the barrier effect of an otherwise porous partially protective film.

1. Introduction

With a constant demand to cut down the fuel consumption and vehicular CO_2 emission, the automobile industry has been in a constant search for greener materials with high strength-to-weight ratio as replacements for the contemporaries and light-weight magnesium alloys perfectly fit the bill. Magnesium being the lightest structural metal, its alloys come-in handy with an attractive combination of low density, good machinability and recyclability. Apart from this mainstream application, magnesium alloys also find scope as electronic, aircraft and bio-implant materials (Agnew, 2004; Cole, 2007; Gupta and Sharon, 2011; Logan, 2007; Luo, 2002). Unfortunately both in electromotive force (EMF) series (De Béthune and Loud, 1964) and galvanic series (Fontana, 1987), pure magnesium appears at active positions, indicating high susceptibility to corrosion, so much so that even aqueous salt media which otherwise act as mild corrosive to majority of metals, severely corrode magnesium alloys and this high susceptibility to corrosion of these alloys jeopardizes their complete utility. ZE41 (Mg–Zn–Zr–RE) is a rare earth containing cast alloy of magnesium, with a scope for applications in several fields. In everyday outdoor applications, this alloy parts encounter corrosives like aqueous salt environments (acid rain and road splash for automobile parts) which bring about severe corrosion of the alloy.

Magnesium alloys when exposed to moist air and aqueous corrosives spontaneously develop a surface film of corrosion product $Mg(OH)_2$. The film however is partially protective due to porosity (Song and Atrens, 1999). While inhibiting

* Corresponding author. Tel.: +91 9448779922; fax: +91 824 2474033.
E-mail address: nityashreya@gmail.com (A.N. Shetty).
Peer review under responsibility of King Saud University.

Production and hosting by Elsevier

http://dx.doi.org/10.1016/j.arabjc.2014.11.028
1878-5352

magnesium corrosion, this naturally formed surface film can be put to good use, by developing inhibitors which enhances the thickness and compactness of already existing surface film, making it more efficient. In this prospect an efficient corrosion inhibitor for magnesium alloys is expected to possess an ability to adsorb as well as precipitate as their sparingly soluble magnesium salts. Yang et al. (2009) proposed that those organic compounds which could form the inhibitor-magnesium precipitation in aqueous solutions could be used as corrosion inhibitors for magnesium alloys. Alkyl carboxylates and surfactants fulfill this requirement. It is proposed that for anionic surfactants the polar head facilitates adsorption onto charged metal surface and the alkyl body forms a compact hydrophobic surface layer (Weisstuch et al., 1971; Zecher, 1976). In this regard several magnesium chelates and surfactants have been explored as magnesium corrosion inhibitors, like ethylenediaminetetraacetic acid (EDTA) (Yang et al., 2009), surfactants like sodium salts of *N*-lauroylsarcosine (NLS), *N*-lauroyl-*N*-methyltaurine (NLT), sodium lauryl sulfate (LS) (Frignani et al., 2012), sodium dodecylbenzenesulfonate (SDBS) (Frignani et al., 2012; Gao et al., 2010; Huang et al., 2011; Li et al., 2009; Yang et al., 2009), and sodium salts of long chain monocarboxylic acids (Duloz et al., 1998; Mesbah et al., 2007).

Stearate is the conjugate base of stearic acid (octadecanoic acid, $(CH_3(CH_2)_{16}COOH)$. Sodium stearate is a major constituent of soaps. Stearate in principle possesses every criterion of an ideal inhibitor for magnesium corrosion, that is stearate is anionic surfactant and readily precipitates as magnesium salt over a wide range of temperatures in aqueous solutions, as witnessed during cleansing in hard water. Magnesium stearate is a major component of "soap scum". Moreover, raw material stearic acid is naturally occurring as triglyceride in tallow, cocoa butter and shea butter. It is renewable, non-toxic, biodegradable and economical. Stearic acid and its derivatives have been investigated for their corrosion inhibition performance toward iron (Gajek et al., 2012; Liu et al., 2006). However, inhibition effect of stearate toward magnesium alloy ZE41 has not been reported so far. The aim of present work is to test the suitability of stearate as inhibitor of ZE41 corrosion in sulfate medium, using electrochemical techniques. It is also intended to study surface morphology using SEM, to investigate the influence of concentration of stearate on inhibition efficiency, to gain an insight into the adsorption process and to propose a suitable mechanism for inhibition.

2. Experimental

2.1. Material

The specimen subjected to corrosion studies was magnesium alloy ZE41. The composition of the sample is as follows (wt%): Zn = 4.49, Ce = 1.05, Zr = 0.7, La = 0.48, Pr = 0.12, Mn = 0.02, Nd < 0.01, Fe = 0.006, Al = 0.004, miner-constituents < 0.002 [Sn, Pb, Cu < 0.002 and Be, Ni, Cr, Sr < 0.001] and the balance is Mg. Cylindrical electrode mounted in epoxy resin with an exposure area of 0.732 cm^2 was polished with SiC papers (of grades in the range 600–2000) and finally mirror finish was obtained with polishing wheel using legated alumina as abrasive. The polished specimen was washed with double distilled water, degreased with acetone and dried properly before immersing in the medium.

2.2. Medium

Sodium sulfate (Na_2SO_4) was used as the corrosion medium. 1.0 M sodium sulfate solution was prepared using analytical grade sodium sulfate salt and double distilled water. The inhibitor sodium stearate as an aqueous solution was prepared by neutralization reaction between equimolar amounts of analytical grade stearic acid and NaOH. Stearate solutions of concentration range 0.5–3.0 mM were prepared in sodium sulfate. Analysis were carried out at temperatures 30 °C, 35 °C, 40 °C, 45 °C and 50 °C (±0.5 °C) using a calibrated thermostat, under unstirred conditions.

2.3. Electrochemical measurements

Electrochemical work station, Gill AC having ACM instrument Version 5 software was employed for carrying out electrochemical measurements. The arrangement adopted was a conventional three-electrode compartment Pyrex glass cell with a platinum counter electrode and a saturated calomel electrode (SCE) as reference. All the values of potential reported are referred to the SCE. The ZE41 alloy specimen coupon was made working electrode. All the electrochemical measurements were carried out in 1.0 M Na_2SO_4 in the absence and presence of inhibitor stearate (0.5–3.0 mM) at temperature intervals as stated in the Section 2.2. The polarization studies were done immediately after the EIS studies on the same exposed electrode surface without subjecting it to any additional surface treatment.

2.3.1. Potentiodynamic polarization studies

The dried and polished ZE41 alloy specimen coupon was exposed to the corrosion medium 1.0 M sodium sulfate at different temperatures (30–50 °C) in the presence and absence of inhibitor stearate. The working electrode was allowed to establish a steady-state open circuit potential (OCP). The potentiodynamic current–potential curves (Tafel curves) were developed by polarizing the specimen to −250 mV cathodically and +250 mV anodically relative to the OCP at a scan rate of 1 mV s^{-1}.

2.3.2. Electrochemical impedance spectroscopy (EIS) studies

In impedance measurements small amplitude (10 mV) sine wave ac voltage with a wide spectrum of frequency ranging from 100 kHz to 0.01 Hz was impressed at OCP. The corrosion behavior was interpreted by analysis of Nyquist and Bode plots. The impedance data of Nyquist plots were fitted with ZSimpWin software version 3.21. The impedance parameters double layer capacitance (C_{dl}), film capacitance (C_f) and film resistance (R_f) were deduced from the analysis.

2.3.3. SEM analysis

The influence of the inhibitor on surface morphology of the ZE41 specimen was established by recording SEM images of the corresponding samples (freshly polished and that immersed in sulfate medium with and without stearate inhibitor) using JEOL JSM-6380LA analytical scanning electron microscope.

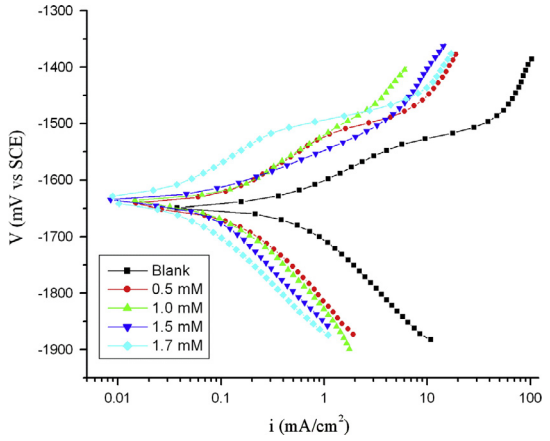

Figure 1 Potentiodynamic polarization curves for the corrosion of ZE41 alloy in 1.0 M Na_2SO_4 containing different concentrations of stearate at 30 °C.

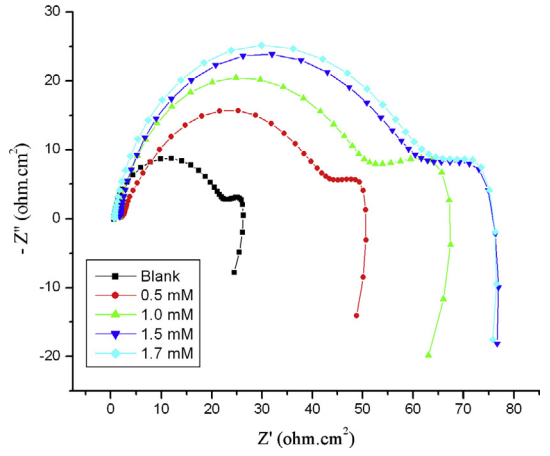

Figure 2 Nyquist plots for the corrosion of ZE41 alloy in 1.0 M Na_2SO_4 containing different concentrations of stearate at 50 °C.

3. Results and discussion

3.1. Potentiodynamic polarization measurements

The Tafel polarization plots for corrosion ZE41 alloy in 1.0 M Na_2SO_4 at 30 °C containing gradually varying concentrations of stearate are represented in Fig. 1. Similar plots were obtained at other temperatures as well. As evidently seen from Tafel plots in Fig. 1, the anodic polarization curves do not exhibit Tafel behavior, possibly because of the disruption of $Mg(OH)_2$ surface film at high anodic over voltage (Song et al., 1997). The anodic branch of Tafel plots is assumed to represent anodic oxidation of magnesium. However cathodic branch of polarization curves showed linear Tafel behavior obeying Tafel equation and thought to represent cathodic hydrogen evolution through reduction of water. The corrosion current density (i_{corr}) was obtained the extrapolation of the cathodic braches of Tafel plot to the OCP. In the presence of stearate the polarization curves shift to lower current density region, which reflects the corrosion inhibition brought about by stearate. However, the shape of Tafel branches remain almost unchanged indicating that stearate neither alters the corrosion mechanism nor participates in electrode reactions instead reduce corrosion rate by blocking active reaction sites on metal surface, most likely by adsorption.

The potentiodynamic polarization parameters like corrosion potential (E_{corr}), corrosion current density (i_{corr}), and cathodic slope (b_c) calculated from the Tafel plots are summarized in Table 1. The corrosion rate (υ_{corr}) shown in Table 1 is calculated using following equation (Eq. (1)) (ASTM Standard G102, 1989).

$$\upsilon_{corr}(\text{mm y}^{-1}) = \frac{K \times i_{corr} \times EW}{\rho} \quad (1)$$

where, constant $K = 0.00327$ mm g/μA cm yr, defines the unit of corrosion rate (mm y^{-1}), i_{corr} is the corrosion current density in μA cm^{-2}, ρ is the density of the corroding material, 1.84 g cm^{-3}, EW is the equivalent weight of the alloy calculated using equation shown below (Eq. (2)).

$$EW = \frac{1}{\Sigma[(n_i \times f_i)/W_i]} \quad (2)$$

where f_i is the weight fraction of the ith element in the alloy, W_i is the atomic weight of the ith element in the alloy and n_i is the valence of the ith element of the alloy (ASTM Standard G102, 1989). The surface coverage θ can be calculated as follows (Eq. (3)).

$$\theta = \frac{i_{corr} - i_{corr(inh)}}{i_{corr}} \quad (3)$$

where i_{corr} and $i_{corr(inh)}$ are corrosion current densities mentioned in identical units in the absence and presence of stearate respectively. The percentage inhibition efficiency ($\eta\%$) is obtained from θ using the equation (Eq. (4)),

$$\eta(\%) = \theta \times 100 \quad (4)$$

3.1.1. Effect of stearate concentration

It is evident from Table 1 that in the presence of stearate i_{corr} decreases, which indicates that corrosion inhibition, is achieved by stearate addition. The η (%) steadily increases with rise in stearate concentration up to an optimum concentration (1.7 mM) above which increase in η (%) is negligible. The increased η (%) with increase in stearate concentration can be attributed to the improved surface coverage. Thus 1.7 mM represents the most economic concentration of stearate for inhibition of ZE41 alloy corrosion, at conditions under consideration. Furthermore the increased stearate concentration results in a gradual and successive anodic shift in E_{corr}, which indicates an anodic type of inhibition. The inhibition action of any inhibitor is considered exclusively as cathodic or anodic when the shift in corrosion potential with respect to OCP of the blank solution is at least −85 mV or +85 mV, respectively (Fekry and Ameer, 2010). However the maximum shift in E_{corr} observed here is +54 mV. A closer observation reveals a very slight change in both the Tafel slopes (b_a and b_c) on addition of stearate, indicating stearate influences kinetics of both anodic metal dissolution and cathodic hydrogen evolution processes. Hence it is safe to say that stearate functions as a mixed-type inhibitor with a predominant anodic control.

Table 1 Electrochemical polarization parameters for the corrosion of ZE41 alloy in 1.0 M Na_2SO_4 containing different concentrations of stearate at different temperatures.

Temperature (°C)	Inhibitor concentration (mM)	E_{corr} (mV/SCE)	i_{corr} (μA cm^{-2})	$-b_c$ (mV dec^{-1})	η (%)
	Blank	−1648	520.78	190	–
	0.5	−1644	145.48	186	72.06
	1.0	−1639	109.53	178	78.97
30	1.5	−1637	67.90	155	86.97
	1.7	−1632	47.92	152	90.79
	1.8	−1626	46.40	149	91.09
	3.0	−1613	39.98	146	92.32
	Blank	−1650	726.69	211	–
	0.5	−1642	242.72	192	66.59
35	1.0	−1639	177.35	184	75.59
	1.5	−1622	122.79	168	83.11
	1.7	−1628	84.06	157	88.43
	Blank	−1657	996.06	228	–
	0.5	−1643	370.52	193	62.81
40	1.0	−1638	307.81	188	69.09
	1.5	−1632	246.25	179	75.28
	1.7	−1627	176.61	163	82.27
	Blank	−1681	1287.70	261	–
	0.5	−1653	555.15	232	56.89
45	1.0	−1642	449.86	196	65.06
	1.5	−1640	402.58	190	68.74
	1.7	−1627	327.09	192	74.59
	Blank	−1686	1451.20	308	–
	0.5	−1669	771.16	269	46.86
50	1.0	−1655	661.05	205	54.45
	1.5	−1654	529.73	201	63.49
	1.7	−1649	506.53	193	65.09

3.2. Electrochemical impedance spectroscopy

EIS undoubtedly is one of the most powerful and sought after technique in electrochemistry, owing to its rich information content, which provides a thorough understanding of electrochemical systems (Mansfeld, 1990). The impedance measurements for the corrosion of ZE41 alloy specimen were carried out under similar conditions as stated in Section 3.1. Fig. 2 presents the Nyquist plots for the corrosion of ZE41 alloy in 1.0 M Na_2SO_4 at 50 °C in the presence of different concentrations of stearate. Similar plots were obtained at other temperatures also. The Nyquist plots were comprised of two capacitive loops at higher and medium frequencies, followed by the beginning of an inductive loop at lower frequency region. The higher frequency (*hf*) semicircle has been attributed to charge transfer of corrosion process and oxide film effects, medium frequency (*mf*) semicircle to mass transport (diffusion) in solid phase through corrosion product layer and lower frequency (*lf*) inductive loop to relaxation of surface adsorbed intermediates like $Mg(OH)^+_{ads}$ and Mg^+_{ads} (Ardelean et al., 2008; Baril and Pebere, 2001; Frignani et al., 2012; Pebere et al., 1990; Zucchi et al., 2006). The enlargement of capacitive loops is indicative of reduced corrosion rate (Pebere et al., 1990). As seen in Fig. 2 with the gradual rise in stearate concentration a successive enlargement of capacitive loops of Nyquist plots resulted without any alterations in shape, which is in agreement with the pattern observed in polarization curves, which imply that stearate reduces corrosion rate without modifying the corrosion mechanism.

The impedance data points neglecting the *lf* inductive loop can be analyzed using an equivalent electrical circuit (EEC) as shown in Fig. 3. The simulation of impedance data points is presented in Fig. 4. The circuit fitment was done by ZSimpWin software of version 3.21. The *hf* response can be simulated by a series of two parallel Resistance-Constant phase element (R-CPE) networks: charge transfer resistance (R_{ct}) in parallel with double layer CPE (Q_{dl}) and resistance of surface film (R_f) in parallel with film CPE (Q_f). The mf response was fitted with a parallel network of resistance (R_{dif}) and CPE (Q_{dif}) associated with diffusion (Fletcher, 1994; Frignani et al., 2012). The capacitive behavior of the system is represented by CPE instead of an ideal capacitor (C) to account for the depressed nature of semicircles. The deviation from ideal capacitive behavior is referred as frequency dispersion and attributed to inhomogeneities of electrode surface (Jüttner, 1990). The

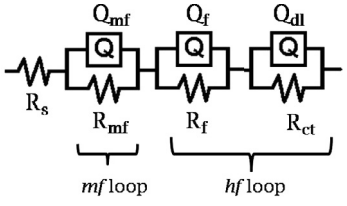

Figure 3 Equivalent electrical circuit used for simulation of experimental impedance data points for the corrosion of ZE41 alloy in 1 M Na_2SO_4 with and without inhibitor stearate.

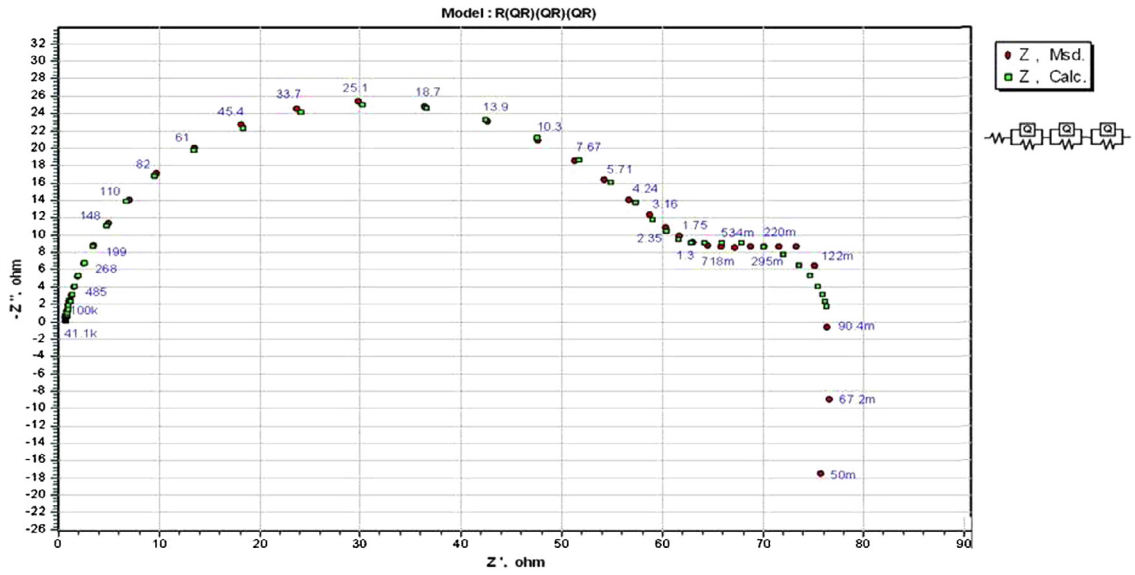

Figure 4 The simulation of experimental impedance data points with theoretical model for corrosion of ZE41 alloy specimen in 1.0 M Na_2SO_4 solution containing 1.7 mM stearate at 50 °C.

impedance of constant phase is described by the expression (Eq. (5)) (Mansfeld et al., 1992):

$$Z_Q = Y_0^{-1}(j\omega)^{-n} \tag{5}$$

where Y_0 is the CPE constant, ω is the angular frequency (in rad s^{-1}), $j^2 = -1$ is the imaginary unit and n is a CPE exponent which is a measure of the heterogeneity or roughness of the surface. The value of n is given by ($-1 \leqslant n \leqslant 1$), CPE simulates an ideal capacitor when $n = 1$, an ideal inductor for $n = -1$, and an ideal resistor for $n = 0$. The capacitance is deduced from CPE using following expression (Eq. (6)) (Mansfeld et al., 1992):

Table 2 Impedance parameters for the corrosion of ZE41 alloy in 1.0 M Na_2SO_4 containing different concentrations of stearate at different temperatures.

Temperature (°C)	Inhibitor concentration (mM)	R_{hf} (Ω cm^2)	R_f (Ω cm^2)	C_{dl} (μF cm^{-2})	C_f (μF cm^{-2})	η (%)
	Blank	46.0	42.0	33.87	108.54	–
	0.5	182.8	128.9	21.14	96.30	74.82
	1.0	204.3	169.5	18.02	84.98	77.47
30	1.5	291.1	186.2	14.81	80.76	84.19
	1.7	497.7	197.8	10.68	71.19	90.75
	1.8	530.6	296.0	9.47	58.33	91.32
	3.0	583.0	556.3	8.14	9.99	92.11
	Blank	39.7	36.2	40.10	108.95	–
	0.5	123.9	120.7	30.23	99.4	67.97
35	1.0	160.3	156.4	27.54	91.95	75.24
	1.5	239.8	174.9	23.10	85.75	83.45
	1.7	324.9	218.1	19.11	74.48	87.79
	Blank	25.0	20.6	42.55	110.19	–
	0.5	64.3	58.5	30.41	104.98	61.11
40	1.0	81.2	72.1	28.46	93.99	69.21
	1.5	106.2	97.9	24.33	87.43	76.58
	1.7	146.1	102.0	22.06	79.56	82.88
	Blank	23.4	18.5	43.16	111.19	–
	0.5	50.7	46.7	34.15	101.9	53.93
45	1.0	66.3	61.2	29.13	99.79	64.77
	1.5	77.8	74.1	26.88	94.92	69.97
	1.7	88.9	81.5	23.62	85.84	73.72
	Blank	22.8	17.4	44.58	115.26	–
	0.5	43.4	40.6	37.88	104.45	47.44
50	1.0	52.9	48.7	33.14	100.45	56.91
	1.5	61.9	57.4	32.71	95.07	63.16
	1.7	67.5	59.6	29.51	87.71	66.21

$$C = Y_0(\omega_m^n)^{n-1} \quad (6)$$

where, ω_m^n is the frequency at which the imaginary part of the impedance (Z'') has a maximum. It has been proposed that the collective resistance associated with *hf* loop is inversely related to corrosion rate (Ardelean et al., 2008; Pebere et al., 1990; Zucchi et al., 2006) and hence the same has been utilized in determination of η (%). The parameters (R_{hf}, C_{dl}, R_f, C_f) deduced from impedance measurements are tabulated in Table 2. η (%) reported in Table 2, was calculated using equation (Eq. (7)) given below (Gao et al., 2011):

$$\eta(\%) = \frac{R_{hf(inh)} - R_{hf}}{R_{hf(inh)}} \times 100 \quad (7)$$

where $R_{hf(inh)}$ and R_{hf} are *hf* loop resistance in the presence of stearate and for blank solution respectively.

It is evidently seen from data in Table 2 that increased stearate amount results in increased R_f and diminution of both C_{dl} and C_f. While R_f is a measure of protective performance of surface film (Zucchi et al., 2006) which enhances on stearate addition, the decrease in C_{dl} and C_f can be attributed to decrease in local dielectric constant and/or increased thickness of electrical double layer and surface film, respectively, as predicted by Helmholtz model (Srinivasan, 2006) (Eq. (8)):

$$C_{dl} = \varepsilon/(4\pi d) \quad (8)$$

where C is the capacitance, ε is local dielectric constant and d is thickness of double layer. The decreased capacitance results from adsorption of stearate along the interface and thickening of $Mg(OH)_2$ surface film. The variation in R_f and C_f collectively suggest formation of a more compact and less defective surface film on addition of stearate. The trend in variation of η (%) with the increase in stearate concentration and the most economic concentration of stearate are in close agreement with those obtained by polarization measurements.

For electrochemical systems with additional time constants, like the present system which demonstrates two relaxation time constants when examined by EIS, Bode phase angle plots are recommended as standard impedance plots, as phase angle (θ) is a sensitive parameter for indicating presence of additional time constants (Badawy et al., 2010). Figs. 5 and 6, respectively, show Bode magnitude and phase angle plots for the corrosion of ZE41 alloy immersed in 1.0 M Na_2SO_4 at 40 °C containing different amounts of stearate. The low frequency impedance modulus (Z_{mod}) and phase maximum at intermediate frequency are the preferential parameters for comparison of the results in Bode magnitude and phase angle plots, respectively Gao et al., 2011). With the increase in stearate concentration, a monotonic increase in Z_{mod} and medium frequency phase maximum can be observed. A larger Z_{mod} demonstrates a better corrosion protection performance and since medium frequency phenomenon is associated with mass transport or diffusion through the defects of $Mg(OH)_2$ surface layer (Gao et al., 2010), the results from Bode magnitude and phase angle plots, respectively, suggest an improved corrosion protection and superior barrier effect against electrolyte ingress.

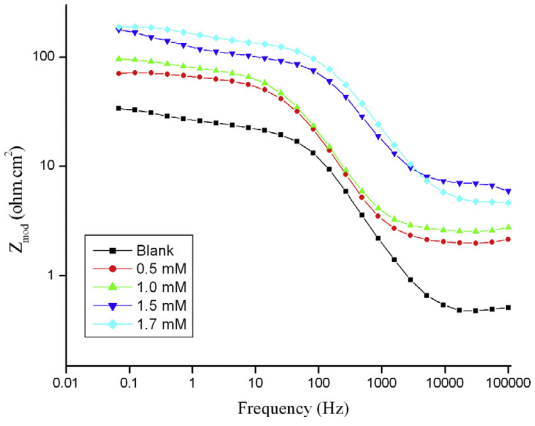

Figure 5 Bode magnitude plots for the corrosion of ZE41 alloy immersed in 1.0 M Na_2SO_4 at 40 °C containing different amounts of stearate.

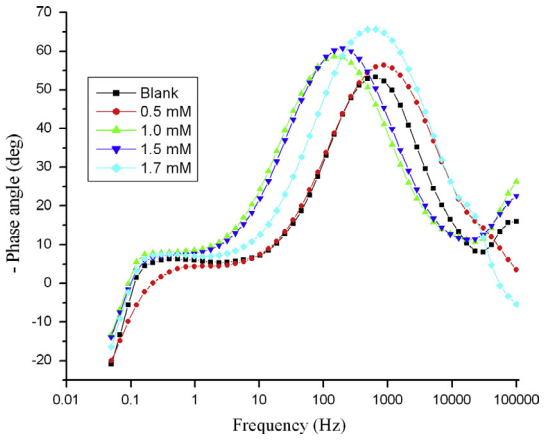

Figure 6 Bode phase angle plots for the corrosion of ZE41 alloy immersed in 1.0 M Na_2SO_4 at 40 °C containing different amounts of stearate.

3.3. Effect of temperature

Temperature is one of the major environmental factors which influence corrosion kinetics as well as action of interfacial inhibitors. The variation in temperature can result in desorption and in some cases even decomposition or rearrangement of organic inhibitors (Antropov, 1967). However the study of the effect of variation in temperature on corrosion inhibition enables deduction of several thermodynamic functions which are helpful in understanding the type of adsorption occurring in the system under study. The data tabulated in Tables 1 and 2, show a steady diminution in inhibition efficiency with the rise in temperature, which is a characteristic feature of physisorption phenomenon. The decrease in η (%) might be attributed to the increased solubility of the magnesium stearate film and it is desorption from the alloy surface (Antropov, 1967; Huang et al., 2011).

Arrhenius law equation (Eq. (9)) which describes temperature dependence of reaction rate has been utilized for calculation of apparent activation energy (E_a) for corrosion in both blank and inhibited systems (Schorr and Yahalom, 1972).

$$\ln(\upsilon_{corr}) = B - \frac{E_a}{RT} \quad (9)$$

where B is a constant depended on the metal type, T is absolute temperature and R is the universal gas constant. The plot of ln (υ_{corr}) versus reciprocal of absolute temperature ($1/T$) presented straight lines with slope = $-Ea/R$ and from the slope the apparent activation energy values for the corrosion process were deduced. Fig. 7 represents the Arrhenius plots for the corrosion of ZE41 alloy specimen 1.0 M Na_2SO_4 containing different concentrations of stearate.

The other thermodynamic functions like apparent enthalpy ($\Delta H^{\#}$) and apparent entropy ($\Delta S^{\#}$) of activation for the alloy dissolution were calculated by application of transition state theory equation (Eq. (10)) (Bentiss et al., 2005).

$$\upsilon_{corr} = \frac{RT}{Nh}\exp\left(\frac{\Delta S^{\#}}{R}\right)\exp\left(\frac{-\Delta H^{\#}}{RT}\right) \quad (10)$$

where h is Planck's constant and N is Avogadro's number. A plot of $\ln(\upsilon_{corr}/T)$ versus $(1/T)$ gives a straight line with slope = $-\Delta H^{\#}/R$ and intercept = $\ln(R/Nh) + \Delta S^{\#}/R$. The plots of $\ln(\upsilon_{corr}/T)$ versus $(1/T)$ for the corrosion of ZE41 alloy specimen in 1.0 M Na_2SO_4 containing varying concentrations of stearate are shown in Fig. 8. The values of $\Delta H^{\#}$ and $\Delta S^{\#}$ calculated from plots in Fig. 8, along with E_a are tabulated in Table 3.

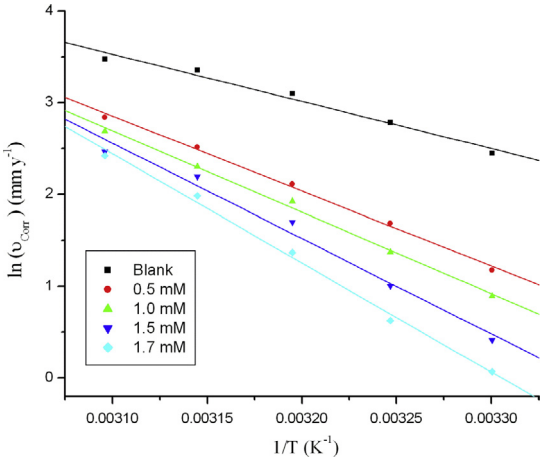

Figure 7 Arrhenius plots for the corrosion of ZE41 alloy in 1.0 M Na_2SO_4 containing different concentrations of stearate.

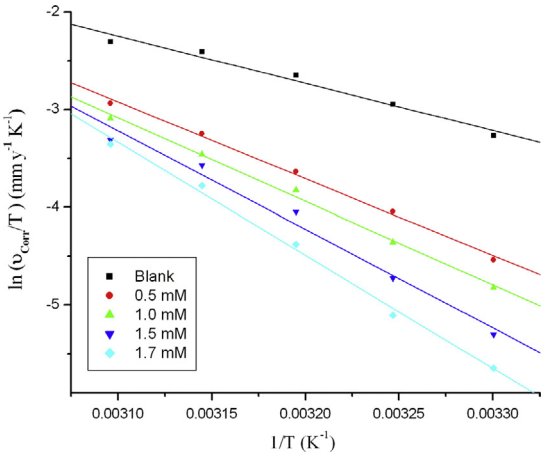

Figure 8 Plots of ln (υ_{corr}/T) *vs* $1/T$ for corrosion of ZE41 alloy in 1.0 M Na_2SO_4 containing different concentrations of stearate.

As observed from the data in Table 3, E_a values are relatively small and increases with the rise in amount of stearate added, which can be attributed to physical adsorption and increased energy barrier for occurrence of corrosion due to the enhanced surface coverage brought about by the inhibitor (Ashassi-Sorkhabi et al., 2005). In both blank and stearate containing systems, the large negative values of $\Delta S^{\#}$ imply that the activated complex in the rate-determining step represents association rather than dissociation, in other words a decrease in randomness takes place when activated complex is formed from reactants (Bentiss et al., 2005; Poornima et al., 2011).

3.4. Adsorption behavior

Majority of organic molecules, especially surfactants act as interfacial inhibitors which bring about corrosion inhibition by adsorption onto metal/electrolyte interface. The inhibitor adsorption on an alloy surface can result from physisorption or chemisorption or both and a thorough understanding of adsorption behavior is helpful in gaining insight into the type of interactions between inhibitor and metal surface and among the adsorbed inhibitor molecules. The adsorption of an interface inhibitor can be viewed as quasi-substitution process between inhibitor in solution and water molecules adsorbed at electrode surface (Damaskin et al., 1972) as follows (Eq. (11));

$$\mathrm{Inh}_{(sol)} + \chi H_2O_{(ads)} \leftrightarrow \mathrm{Inh}_{(ads)} + \chi H_2O_{(sol)} \quad (11)$$

where χ represents the number of water molecules replaced by one inhibitor molecule on adsorption, and χ is often termed as size ratio.

Traditionally the extent of corrosion inhibition by interfacial inhibitors is analyzed as a function of surface coverage (θ). The values of θ at different stearate concentrations (C_{inh}) were calculated from the results of polarization studies using previously mentioned relations (Eqs. (3) and (4)). Efforts were made to graphically fit the values of θ and C_{inh} to various adsorption isotherms with an aim to obtain a liner relationship. The results presented best agreement with the Langmuir adsorption isotherm, which can be mathematically represented as follows (Eq. (12)),

$$\frac{C_{inh}}{\theta} = C_{inh} + \frac{1}{K} \quad (12)$$

where K is the equilibrium constant for adsorption–desorption process. For an ideal Langmuir adsorption phenomenon the

Table 3 Activation parameters for the corrosion of ZE41 alloy in 1.0 M Na_2SO_4 containing different concentrations of stearate.

Inhibitor concentration (mM)	Ea (kJ mol^{-1})	$\Delta H^{\#}$ (kJ mol^{-1})	$\Delta S^{\#}$ (J mol^{-1} K^{-1})
0	42.76	40.16	−174.89
0.5	67.84	65.24	−102.75
1.0	73.73	71.13	−85.84
1.5	86.44	83.83	−47.56
1.7	98.86	96.26	−10.02

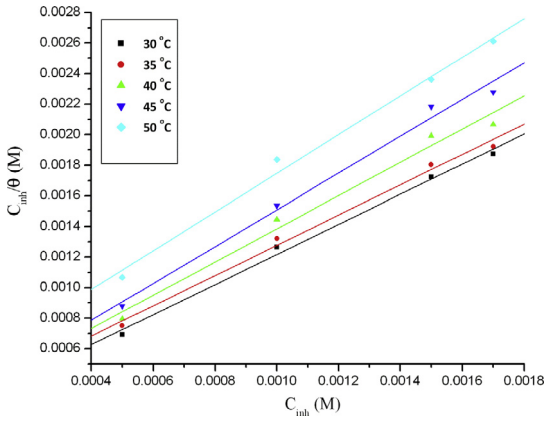

Figure 9 The Langmuir adsorption isotherms for adsorption of stearate on ZE41 alloy surface at different temperatures.

plot of (C_{inh}/θ) versus C_{inh} gives a straight line with ($1/K$) as the intercept and slope equal to unity. The Langmuir adsorption isotherms for the adsorption of stearate on ZE41 alloy surface at different temperatures are presented in Fig. 9. The plots exhibit linear behavior; however the slopes are not equal to unity. The average linear regression coefficient (R^2) of 0.99 was obtained. This deviation from ideal Langmuir behavior can be attributed to mutual interaction among the adsorbed species (Poornima et al., 2011).

The standard free energy of adsorption ($\Delta G°_{ads}$) is related to K by the reaction isotherm equation (Eq. (13)) as shown below (Poornima et al., 2011).

$$\Delta G°\text{ads} = -RT\ln(55.5 * K) \tag{13}$$

where 55.5 in mol dm^{-3} is the concentration of water in solution, T is absolute temperature and R is the universal gas constant. From the plot of $\Delta G°_{ads}$ versus T, the other thermodynamic functions like standard enthalpy of adsorption ($\Delta H°_{ads}$) and standard entropy of adsorption ($\Delta S°_{ads}$), can be calculated using thermodynamic relation (Eq. (14)),

$$\Delta G°_{ads} = \Delta H°_{ads} - T\Delta S°_{ads} \tag{14}$$

All the thermodynamic parameters for the adsorption of stearate on ZE41 alloy surface are tabulated in Table 4. From these parameters some valuable information about overall process of adsorption can be derived. The negative values of $\Delta G°_{ads}$ imply that the process of adsorption of stearate is spontaneous and stearate as an adsorbed layer on the alloy surface is stable. Usually physisorption processes are accompanied with lower $\Delta G°_{ads}$ values below -20 kJ mol^{-1} and chemisorption on the other hand involves a higher $\Delta G°_{ads}$ above -40 kJ mol^{-1} (Bentiss et al., 2005; Poornima et al., 2011; Sanathkumar et al., 2012). The intermediate values of $\Delta G°_{ads}$ (-31 to -32 kJ mol^{-1}) obtained in the study suggest that interactions between stearate molecules and surface atoms of the alloy comprise of both electrostatic forces and coordinate covalent bonding resulting respectively in both physical and chemical adsorption. The negativity of $\Delta H°_{ads}$ signifies that the process of stearate adsorption is exothermic. The exothermic nature of adsorption can arise as a result of physisorption or chemisorption; however endothermic adsorption is a feature exclusively associated with chemisorption. In cases of exothermic adsorption physisorption is distinguished from chemisorption based on the absolute value of adsorption enthalpy. The typical adsorption enthalpy for physisorption is -40.86 kJ mol^{-1} and that for chemisorption is -100 kJ mol^{-1} (Martinez and Stern, 2002). The value of $\Delta H°_{ads}$ obtained for stearate adsorption is -44.41 kJmol^{-1}, which is close to adsorption enthalpy threshold for physisorption. A large negative value of $\Delta S°_{ads}$ equal to -44 J K^{-1} mol^{-1} suggests that the entropy of the system decrease during stearate adsorption. This diminution in disorderliness arises because randomly moving stearate molecules in solution form an orderly arranged molecular layer upon adsorption (Poornima et al., 2011).

3.5. Mechanism of corrosion inhibition

A thorough understanding of mechanism of magnesium corrosion and surfactant aggregation is essential before arriving at a conclusive inhibition mechanism. In this regard it is intended to briefly discuss some fundamental aspects.

3.5.1. Micro-galvanic corrosion of alloy ZE41

As per previously reported studies (Coy et al., 2010; Neil et al., 2009) the microstructure of as-cast ZE41 alloy to comprises of the α-Mg matrix which forms the body of the grain and secondary phases like β-phase particles irregularly distributed within the grains and the T-phase distributed eutectic alloy at the grain boundaries. The β-phase particles are found to be rich in zirconium (Zr_4Zn) and T-phase comprised of rare earth elements (Mg_7Zn_3RE). These intermetallic secondary phases act as cathodes to neighboring α-Mg matrix. Thus in the presence of a suitable corrosive, ZE41 undergoes severe localized micro-galvanic corrosion, where α-Mg matrix corrodes as anode and β-phase and T-phase are protected as cathode.

Greenblatt (1956) suggested the following overall reaction for self corrosion of magnesium in aqueous solutions.

$$Mg + 2H_2O \rightarrow Mg(OH)_2 + H_2 \tag{15}$$

The cathodic reaction in neutral or alkaline solutions involves hydrogen evolution by electrochemical reduction of water.

$$2H_2O + 2e^- \rightarrow H_{2(g)} + 2OH^- \tag{16}$$

Table 4 The thermodynamic parameters for adsorption of stearate on ZE41 alloy surface in 1 M Na_2SO_4.

Temperature (°C)	K (mol^{-1} dm^3)	$\Delta G°_{ads}$ (kJ mol^{-1})	R^2	$\Delta H°_{ads}$ (kJ mol^{-1})	$\Delta S°_{ads}$ (J mol^{-1} K^{-1})
30	4289	−31.19	0.994		
35	3465	−31.16	0.992		
40	3333	−31.56	0.984	−44.41	−44.00
45	3268	−32.01	0.991		
50	2069	−31.29	0.992		

The anodic dissolution of magnesium however comprises of multiple steps with several intermediates involved (Baghni et al., 2004). At active potentials around −2.78 V (vs SCE) magnesium is oxidized to monovalent magnesium ions (Mg^+) and at slightly higher potentials of −1.56 V (vs SCE) oxidation to divalent magnesium ions (Mg^{2+}) occurs in parallel with the former oxidation step (Cai et al., 2009; Lopez and Natta, 2001) as shown below.

$$Mg \rightarrow Mg^+ + e^- \quad (17)$$

$$Mg \rightarrow Mg^{2+} + 2e^- \quad (18)$$

The Mg^+ is highly unstable and readily oxidizes to Mg^{2+}. This secondary oxidation proceeds in multiple steps ultimately forming principal corrosion product $Mg(OH)_2$ (Cai et al., 2009).

$$2Mg^+ + 2H_2O \rightarrow Mg^{2+} + Mg(OH)_2 + H_2 \quad (19)$$

$$Mg^+ + 2H^+ + 3e^- \rightarrow MgH_2 \quad (20)$$

$$MgH_2 + 2H_2O \rightarrow Mg^{2+} + 2OH^- + 2H_2 \quad (21)$$

$$Mg^{2+} + 2OH^- \rightarrow Mg(OH)_2 \quad (22)$$

Thus during magnesium corrosion in aqueous solutions the evolution of hydrogen occurs not just electrically by reduction at cathode but also chemically during oxidation of Mg^+ to Mg^{2+}. The chemical evolution of hydrogen at anode is one of the explanations among the several mechanisms proposed to explain the strange anodic dissolution of magnesium referred to as Negative Difference Effect (NDE) (Song et al., 1997).

The accumulation of magnesium hydride (MgH_2) takes place when the rate of its formation (Eq. (20)) is faster than its oxidation (Eq. (21)). While this phenomenon of hydride formation as well as evolution of immense volume of hydrogen during magnesium corrosion is used constructively in hydrogen energy technology (Anik, 2012; Darriet et al., 1980; Uan et al., 2009; Vojtech et al., 2009; Yu et al., 2012), the same can be devastating in applications where magnesium alloys are used as structural materials e.g. automobiles and aircrafts.

The corrosion product $Mg(OH)_2$ preferentially precipitates over the regions with sufficient dissolved Mg^{2+} ions. Thus a layer of deposits is more likely to form on α-Mg matrix than on β-phase and T-phases, in other words the continuity of surface film is disrupted by cathodic intermetallics (Huang et al., 2011). This spontaneously developed surface layer offers certain degree of protection (primary inhibition) to underlying alloy; however its effectiveness is inadequate due to high porosity and instability at higher temperatures. Several studies have reported the $Mg(OH)_2$ surface layer to be partially protective, with corrosion reactions occurring predominantly at the breaks and imperfections of the film (Song and Atrens, 1999, 2003; Zhao et al., 2008).

3.5.2. Stearate aggregation at alloy/electrolyte interface

Monolayers of stearate and other fatty acids salts have been investigated in great detail in the past, both as Langmuir layers at the air–water interface (Yazdanian et al., 1992; Bloch et al., 1988; Gericke and Huehnerfuss, 1993) and as Langmuir Blodgett films deposited onto solid surfaces (Ye et al., 2003, 2004) dating back all the way to the original work of Blodgett (1935) and Langmuir (1938). It is well known that both the physical and chemical properties of such layers depend very much on the ion content of an adjacent aqueous phase (Aveyard et al., 1990). While investigating the inhibition property of a surfactant, stearate in this case, the tendency of surfactant molecules to associate with one another both in solutions and at interfaces cannot be overlooked. For surfactant adsorption at air–water interface, critical micelle concentration (CMC) marks the concentration threshold below which surfactants exist in monomeric state and above which they self-aggregate to form spherical micelles. The analog to micelles in solutions is bilayers or multilayers at solid surfaces. The concentration limit above which the transition from monolayer to multilayer occurs at solid-solution interface is termed as aggregate transition concentration (ATC). Free (2004) reported that ATC is similar and analogous to CMC and often occurs at concentrations of same order of magnitude as CMC and any difference in magnitude between the two is attributed to difference in interaction energies of solid–liquid and air–liquid interfaces with surfactant molecules.

Thus during corrosion inhibition by surfactants, ATC marks an effective boundary condition. It is observed that up to ATC the surfactant added increasingly cover the surface in the form of a monolayer and η (%) increase with increased surfactant concentration. At ATC a complete monolayer formed is adequate for significant inhibition and increased concentration above ATC, forms multilayers of surfactants, which further increases η (%) but to a negligible extent (Free, 2002). Fig. 10 shows a plot of $(1/i_{corr})$ versus concentration of stearate, ATC of 1.7 mM is located as the concentration at which a steep slope changes sharply into a gradual slope.

Thus for inhibition involving surfactants the efficiency should always be related to effective surface coverage rather than physical coverage (Free, 2004) as assumed by Langmuir adsorption isotherm model. In other words the traditional analysis of corrosion inhibition as a function of surface coverage is applicable only below ATC and Langmuir adsorption isotherm which models a monolayer adsorption is not obeyed above ATC.

3.5.3. Corrosion inhibition by stearate

Based on comprehensive results of the study the following mechanism of inhibition has been proposed. Stearate is anionic surfactant with a capability to both physically and chemically

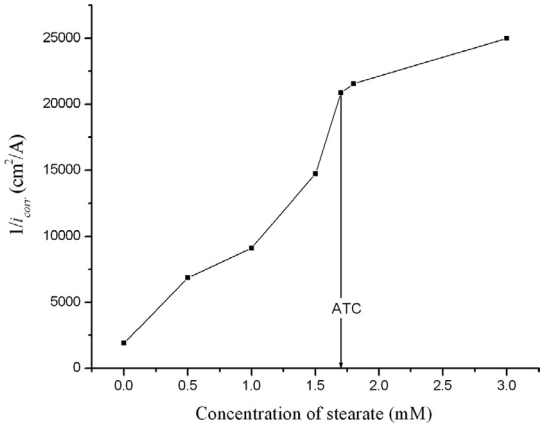

Figure 10 The plot of $(1/i_{corr})$ *vs* concentration of stearate for the corrosion of ZE41 alloy in 1.0 M Na_2SO_4 at 30 °C.

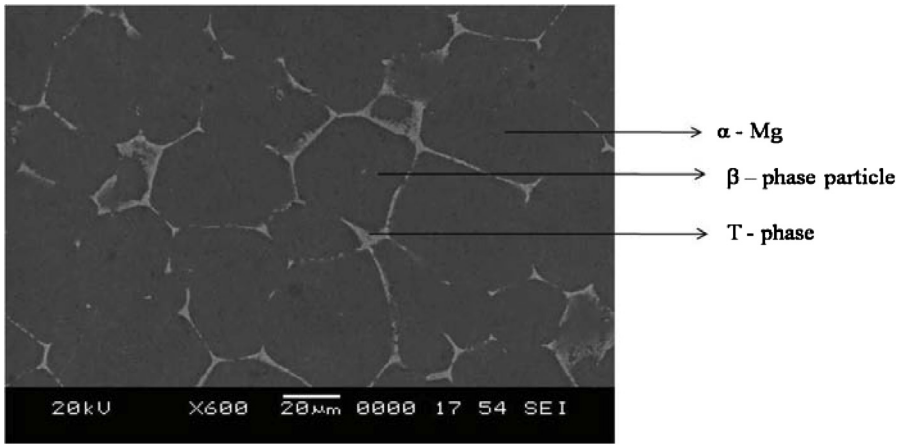

(a)

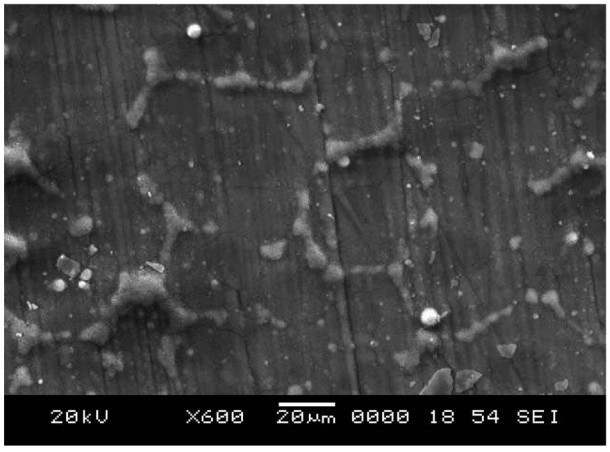

(b)

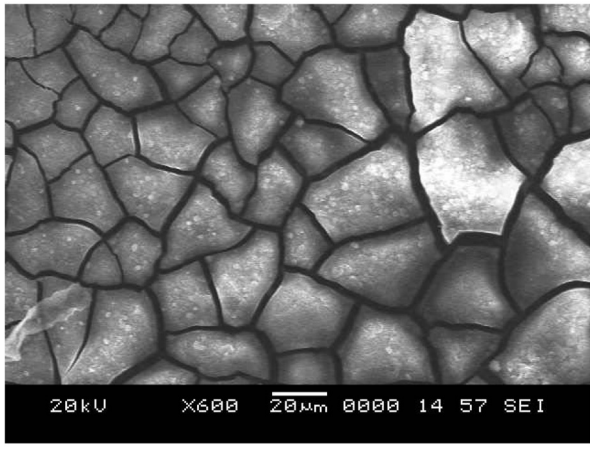

(c)

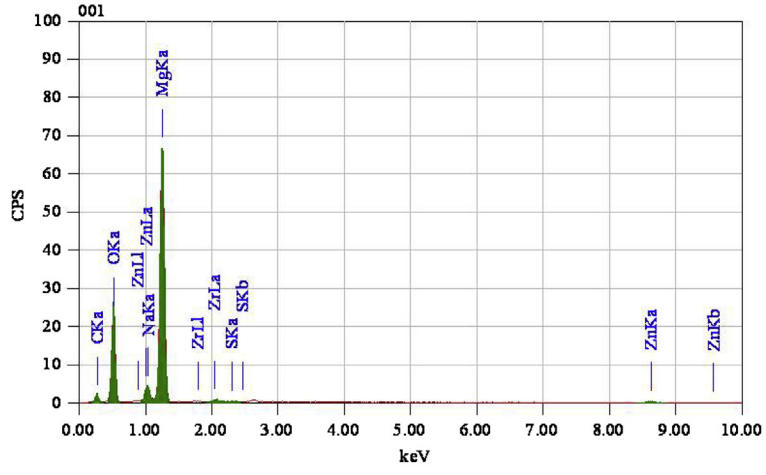

(d)

Figure 11 SEM image of ZE41 alloy specimen (a) freshly polished surface, (b) after 1 h immersion in blank 1.0 M Na_2SO_4, (c) after 1 h immersion in 1.0 M Na_2SO_4 containing 1.7 mM of stearate, (d) EDX spectrum of ZE41 specimen surface after 1 h immersion in the medium of 1.0 M Na_2SO_4 solutions containing 1.7 mM of stearate.

adsorb on to ZE41 alloy surface. The physisorption can arise from electrostatic interactions between anionic carboxylate group of stearate and Mg^{2+} ions trapped within the pores and defects of $Mg(OH)_2$ surface film developed over α-Mg matrix and chemisorption on the other hand is prominent at film free surfaces which are cathodic intermetallic phases (β-phase and grain boundary T-phase), where stronger covalent bonds are formed by donor-accepter interactions between

unshared electron pairs of oxygen of carboxylate and vacant d-orbitals of Zr or RE metal atoms (Huang et al., 2011). The physisorbed stearate over α-Mg matrix subsequently precipitates as Mg-stearate owing to its very low solubility product. The precipitation of Mg-stearate makes the surface layer much compact by reducing the porosity and imperfections and it also imparts a certain degree of hydrophobicity to surface film, which is desirable (Frignani et al., 2012). The van der Waals interactions between long alkyl chains of adsorbed stearate molecules further improves the compactness of the film. A more compact modified surface film over α-Mg matrix reduces anodic Mg dissolution through an enhanced barrier effect against electrolyte ingress. The chemisorbed stearate at cathodic intermetallic phases reduces the rate of cathodic hydrogen evolution by blocking active cathodic reaction sites (Zucchi et al., 2009).

In general with increased temperature the extent of physisorption decreases due to desorption and that of chemisorption increases, which is also termed as activated adsorption. The thermodynamic parameters derived in this study suggested occurrence of both physisorption and chemisorptions. However, a close proximity of ΔH°_{ads} to adsorption enthalpy threshold for physisorption and a prominent decrease in η (%) with rise in temperature collectively imply the predominance of physisorption. At higher temperature Mg^{2+} ions diffuse faster and farther even to cathodic regions which are sites of chemisorption. The availability Mg^{2+} ions at cathodic regions favor a more instantaneous physisorption of stearate than chemisorption. Hence the Mg-stearate film deposited through physisorption tends to migrate to whole alloy surface at higher temperatures (Huang et al., 2011). The trend of reduction in η (%) with rise in temperature can be attributed to a more pronounced predominance of physisorption over chemisorption at higher temperature, desorption of physisorbed stearate and increased solubility of Mg-stearate. Like any other chemical reaction rate of electrochemical corrosion irrespective of presence or absence of inhibitor, will usually increase with the rise in temperature and at metal surface a more frequently evolving hydrogen might also interfere with adsorption process (Sanathkumar et al., 2012).

The most economic concentration of stearate corresponding to its ATC reflects that a significant protection is provided by monolayer and the additional contribution of bilayers or multilayers toward inhibition is negligible. This phenomenon has been supported by study conducted by Xing et al. (1995); using transferred Langmuir–Blodgett films of stearic acid on iron surface, where original monolayer provided inhibition efficiency of 65% and each supplementary monolayer added onto original monolayer resulted in an additional increase in inhibition efficiency by 4%. This behavior can be explained by considering the mode of inhibition by monolayer and multilayers. Up to ATC added surfactant molecules effectively cover the alloy surface, block the active electrode reaction sites and also offer certain resistance to electrolyte ingress. However above ATC added surfactants do not have direct access to alloy surface instead these molecules build up additional layers and augment the resistance to molecular transport. A drastically high film resistance (R_f) and notably low film capacitance (C_f) at 3.0 mM concentration of stearate (well above ATC) further supports the explained mechanism.

3.6. Surface morphology: SEM analysis

The surface morphology was analyzed using scanning electron microscopy to further investigate the inhibitive effect of stearate. Fig. 11(a) shows the SEM image of a freshly polished surface of ZE41 alloy. The microstructure of the alloy comprising of α-Mg matrix, β-phase particles and grain boundary T-phase, is evident. Fig. 11(b and c) are the SEM image of ZE41 specimen surface after 1 h immersion in blank 1.0 M Na_2SO_4 and 1.0 M Na_2SO_4 containing 1.7 mM of stearate. The corroded surface in the absence of inhibitor stearate shows the existence of $Mg(OH)_2$ surface film. The surface film has a characteristic "mud cracking" appearance, which is more pronounced due to dehydration of the film by drying and vacuum application in SEM chamber (Neil et al., 2009). The film appears highly porous and non-uniform which substantiates its partially protective behavior. The protected alloy surface in the presence of stearate once again exhibits the surface film with "mud cracking" appearance; however the film appears highly compact and uniform which further validates the mechanism of inhibition by adsorption and formation of compact modified surface film. EDX spectrum of ZE41 specimen surface after 1 h immersion in the medium of 1.0 M Na_2SO_4 solutions containing 1.7 mM of stearate is shown in Fig. 11(d). The spectrum consists of a carbon peak, indicating the presence of carbon on the surface of the alloy. Though the intensity of the carbon peak is low, it still cannot be ignored and such a peak indicate the presence of some organic moieties on the alloy surface which in all likelihood are the surface adsorbed stearate molecules.

4. Conclusions

- The anionic surfactant stearate acts as an appreciably good inhibitor of magnesium alloy ZE41 corrosion in aqueous sulfate medium.
- The polarization studies indicate that stearate functions as a mixed-type corrosion inhibitor with a predominant control over anodic metal dissolution reaction.
- The inhibition efficiency noticeably increases with the increase in stearate concentration up to aggregate transition concentration, beyond which the rise in the inhibition efficiency is insignificant.
- The inhibition efficiency decreases with the increase in temperature, although stearate does act as a moderate inhibitor at higher temperature.
- The adsorption of stearate on alloy surface is predominantly physisorption and follows the Langmuir adsorption isotherm.
- The inhibition efficiencies calculated from polarization and impedance measurements are in reasonably good agreement.

References

Agnew, S.R., 2004. Wrought magnesium: a 21st century outlook. JOM 56, 20–21.

Anik, M., 2012. Improvement of the electrochemical hydrogen storage performance of magnesium based alloys by various additive elements. Int. J. Hydrogen Energy 37, 1905–1911.

Antropov, L.I., 1967. A Correlation between kinetics of corrosion and the mechanism of inhibition by organic compounds. Corros. Sci. 7, 607–620.
Ardelean, H., Frateur, I., Marcus, P., 2008. Corrosion protection of magnesium alloys by cerium, zirconium and niobium-based conversion coatings. Corros. Sci. 50, 1907–1918.
Ashassi-Sorkhabi, H., Ghasemi, Z., Seifzadeh, D., 2005. The inhibition effect of some amino acids towards the corrosion of aluminum in 1 M HCl + 1 M H_2SO_4 solution. Appl. Surf. Sci. 249, 408–418.
ASTM Standard G102, 1989(1999). Standard Practice for Calculation of Corrosion Rates and Related Information From Electrochemical Measurements. ASTM International, West Conshohocken, PA.
Aveyard, R., Binks, B.P., Carr, N., Cross, A.W., 1990. Stability of insoluble monolayers and ionization of Langmuir-Blodgett multilayers of octadecanoic acid. Thin Solid Films 188, 361–373.
Badawy, W.A., Hilal, N.H., El-Rabiee, M., Nady, H., 2010. Electrochemical behavior of Mg and some Mg alloys in aqueous solutions of different pH. Electrochim. Acta 55, 1880–1887.
Baghni, M., Wu, Y., Li, J., Zhang, W., 2004. Corrosion behavior of magnesium and magnesium alloys. Trans. Nonferrous Met. Soc. China 14, 1–10.
Baril, G., Pebere, N., 2001. The corrosion of pure magnesium in aerated and deaerated sodium sulphate solutions. Corros. Sci. 43, 471–484.
Bentiss, F., Lebrini, M., Lagrenee, M., 2005. Thermodynamic characterization of metal dissolution and inhibitor adsorption processes in mild steel/2,5-bis(n-thienyl)-1,3,4-thiadiazoles/hydrochloric acid system. Corros. Sci. 47, 2915–2931.
Bloch, J.M., Yun, W.B., Yang, X., Ramanathan, M., Montano, P.A., Capasso, C., 1988. Adsorption of counterions to a stearate monolayer spread at the water-air interface; a synchrotron X-ray study. Phys. Rev. Lett. 61, 2941–2944.
Blodgett, K.B., 1935. Films built by depositing successive monomolecular layers on a solid surface. J. Am. Chem. Soc. 57, 1002–1022.
Cai, Z., Lu, D., Li, W., Liang, Y., Zhou, H., 2009. Study on anodic oxidation of magnesium in 6 M KOH solution by alternative current impedance. Int. J. Hydrogen Energy 34, 467–472.
Cole, G., 2007. Summary of Magnesium Vision 2020: A North American Automotive Strategic Vision for Magnesium. In: Beals, R.S., Luo, A.A., Neelameggham, N.R., Pekguleryuz, M.O. (Eds.), Magnesium Technology. TMS, Warrendale, Pennsylvania, p. 35.
Coy, A.E., Viejo, F., Skeldon, P., Thompson, G.E., 2010. Susceptibility of rare-earth-magnesium alloys to micro-galvanic corrosion. Corros. Sci. 52, 3896–3906.
Damaskin, B.B., Petrii, O.A., Batrakov, V.V., Uvarov, E.B., Parsons, R., Barradas, R.G., 1972. Adsorption of organic compounds on electrodes. J. Electrochem. Soc. 119, 279–280.
Darriet, B., Pezat, M., Hbika, A., Hagenmuller, P., 1980. Application of magnesium rich rare-earth alloys to hydrogen storage. Int. J. Hydrogen Energy 5, 173–178.
De Béthune, A.J., Loud, N.A.S., 1964. Standard aqueous electrode potentials and temperature coefficients at 25 °C. Clifford A. Hampel., Skokie, IL.
Duloz, D., Rapin, C., Steinmetz, P., Michot, G., 1998. Corrosion inhibition of rapidly solidified Mg–3%Zn–15%Al magnesium alloy with sodium carboxylates. Corrosion. 54, 444–450.
Fekry, A.M., Ameer, M.A., 2010. Corrosion inhibition of mild steel in acidic media using newly synthesized heterocyclic organic molecules. Int. J. Hydrogen Energy 35, 7641–7651.
Fletcher, S., 1994. Tables of degenerate electrical networks for use in the equivalent-circuit analysis of electrochemical systems. J. Electrochem. Soc. 141, 1823–1826.
Fontana, M.G., 1987. Corrosion Engineering. McGraw Hill, Singapore, pp. 42–43.
Free, M., 2002. Understanding the effect of surfactant aggregation on corrosion inhibition of mild steel in acidic medium. Corros. Sci. 44, 2865–2870.
Free, M., 2004. A new corrosion inhibition model for surfactants that more closely accounts for actual adsorption than traditional models that assume physical coverage is proportional to inhibition. Corros. Sci. 46, 3101–3113.
Frignani, A., Grassi, V., Zanotto, F., Zucchi, F., 2012. Inhibition of AZ31 Mg alloy corrosion by anionic surfactants. Corros. Sci. 63, 29–39.
Gajek, A., Zakroczymski, T., Romanchuk, V., Topilnytsky, P., 2012. Protective properties and spectral analysis of nitrogen- and oxygen-containing corrosion inhibitors for oil equipment. Chem. Chem. Technnol. 6, 209–217.
Gao, H., Li, Q., Dai, Y., Luo, F., Zhang, H.X., 2010. High efficiency corrosion inhibitor 8-hydroxyquinoline and its synergistic effect with sodium dodecylbenzenesulphonate on AZ91D magnesium alloy. Corros. Sci. 52, 1603–1609.
Gao, H., Li, Q., Chen, F.N., Dai, Y., Luo, F., Li, L.Q., 2011. Study of the corrosion inhibition effect of sodium silicate on AZ91D magnesium alloy. Corros. Sci. 53, 1401–1407.
Gericke, A., Huehnerfuss, H., 1993. In-situ investigation of saturated long-chain fatty acids at the air/water interface by external infrared reflection-absorption spectrometry. J. Phys. Chem. 97, 12899–12908.
Greenblatt, J.H., 1956. A mechanism for the anodic dissolution of magnesium. J. Electrochem. Soc. 103, 539–543.
Gupta, M., Sharon, N.M.L., 2011. Magnesium, Magnesium Alloys and Magnesium Composites. John Wiley & Sons, New Jersy.
Huang, D., Hu, J., Song, G.-L., Guo, X., 2011. Inhibition effect of inorganic and organic inhibitors on the corrosion of Mg–10Gd–3Y–0.5Zr alloy in an ethylene glycol solution at ambient and elevated temperatures. Electrochim. Acta 56, 10166–10178.
Jüttner, K., 1990. Electrochemical impedance spectroscopy (EIS) of corrosion processes on inhomogeneous surfaces. Electrochim. Acta 35, 1501–1508.
Langmuir, I., 1938. Overturning and anchoring of monolayers. Science 87, 493–500.
Li, L.J., Yao, Z.M., Lei, J.L., Xu, H., Zhang, S.T., Pang, F.S., 2009. Adsorption and corrosion behaviour of sodium dodecylbenzenesulfonate on AZ31 magnesium alloy. Acta Phys. Chim. Sin. 25, 1332–1336.
Liu, X., Chen, S., Ma, H., Liu, G., Shen, L., 2006. Protection of iron corrosion by stearic acid and stearic imidazoline self-assembled monolayers. Appl. Surf. Sci. 253, 814–820.
Logan, S.D., 2007. Lightweight Automobile Body Concept Featuring Ultra-Large, Thin-Wall Structural Magnesium Castings. In: Beals, R.S., Luo, A.A., Neelameggham, N.R., Pekguleryuz, M.O. (Eds.), Magnesium Technology. TMS, Warrendale, Pennsylvania, p. 41.
Lopez, M.G., Natta, B., 2001. Evidence of two anodic processes in the polarization curves of magnesium in aqueous media. Corrosion. 712, 5006–5015.
Luo, A.A., 2002. Magnesium: current and potential automotive applications. JOM 54, 42–48.
Mansfeld, F., 1990. Electrochemical impedance spectroscopy (EIS) as a new tool for investigating methods of corrosion protection. Electrochim. Acta 35, 1533–1544.
Mansfeld, F., Tsai, C.H., Shih, H., 1992. Software for simulation and analysis of electrochemical impedance spectroscopy (EIS) data. In: Munn, R.S. (Ed.), Computer modeling in corrosion. ASTM, Philadelphia, pp. 186–196.
Martinez, S., Stern, I., 2002. Thermodynamic characterization of metal dissolution and inhibitor adsorption processes in the low carbon steel/mimosa tannin/sulfuric acid system. Appl. Surf. Sci. 199, 83–89.
Mesbah, A., Juers, C., Lacouture, F., Mathieu, S., Rocca, E., Francois, M., Steinmetz, J., 2007. Inhibitors for magnesium corrosion: metal-organic frameworks. Solid State Sci. 9, 322–328.
Neil, W.C., Forsyth, M., Howlett, P.C., Hutchinson, C.R., Hinton, B.R.W., 2009. Corrosion of magnesium alloy ZE41 – The role of microstructural features. Corros. Sci. 51, 387–394.

Pebere, N., Riera, C., Dabosi, F., 1990. Investigation of magnesium corrosion in aerated sodium sulfate solution by electrochemical impedance spectroscopy. Electrochim. Acta 35, 555–561.

Poornima, T., Nayak, J., Shetty, A.N., 2011. Effect of 4-(N,N-diethylamino) benzaldehyde thiosemicarbazone on the corrosion of aged 18 Ni 250 grade maraging steel in phosphoric acid solution. Corros. Sci. 53, 3688–3696.

Sanathkumar, B.S., Nayak, J., Shetty, A.N., 2012. Influence of 2-(4-chlorophenyl)-2-oxoethyl benzoate on the hydrogen evolution and corrosion inhibition of 18 Ni 250 grade weld aged maraging steel in 1.0 M sulfuric acid medium. Int. J. Hydrogen Energy 37, 9431–9442.

Schorr, M., Yahalom, J., 1972. The significance of the energy of activation for the dissolution reaction of metal in acids. Corros. Sci. 12, 867–868.

Song, G., Atrens, A., 1999. Corrosion mechanisms of magnesium alloys. Adv. Eng. Mater. 1, 11–33.

Song, G., Atrens, A., 2003. Understanding magnesium corrosion—a framework for improved alloy performance. Adv. Eng. Mater. 5, 837–858.

Song, G., Atrens, A., StJohn, D., Nairn, J., Li, Y., 1997. The electrochemical corrosion of pure magnesium in 1 N NaCl. Corros. Sci. 39, 855–875.

Srinivasan, S., 2006. Electrode/Electrolyte Interfaces: Structure and Kinetics of Charge Transfer, Fuel Cells: From Fundamentals to Applications. Springer, New York, p. 28.

Uan, J.Y., Yu, S.H., Lin, M.C., Chen, L.F., Lin, H.I., 2009. Evolution of hydrogen from magnesium alloy scraps in citric acid-added seawater without catalyst. Int. J. Hydrogen Energy 34, 6137–6142.

Vojtech, D., Sustarsic, B., Mortanikova, M., Michalcova, A., Vesela, A., 2009. Electrochemical hybriding as method for hydrogen storage. Int. J. Hydrogen Energy 34, 7239–7245.

Weisstuch, A., Carter, D.A., Nathan, C.C., 1971. Chelation compounds as cooling water corrosion inhibitors. Mater. Prot. Perform. 10, 11–15.

Xing, W., Shan, Y., Guo, D., Lu, T., Xi, S., 1995. Mechanism of iron inhibition by stearic acid Langmuir-Blodgett monolayers. Corrosion. 51, 45–49.

Yang, X., Pan, F.S., Zhang, D.F., 2009. A study on corrosion inhibitor for magnesium alloy. Mater. Sci. Forum 610, 920–926.

Yazdanian, M., Yu, H., Zografi, G., Kim, M.W., 1992. Divalent cation-stearic acid monolayer interactions at the air/water interface. Langmuir 8, 630–636.

Ye, S., Noda, H., Morita, S., Uosaki, K., Osawa, M., 2003. Surface molecular structures of Langmuir-Blodgett films of stearic acid on solid substrates studied by sum frequency generation spectroscopy. Langmuir 19, 2238–2242.

Ye, S., Noda, H., Nishida, T., Morita, S., Uosaki, K., Osawa, M., 2004. Cd^{2+} induced interfacial structural changes of Langmuir-Blodgett films of stearic acid on solid substrates: A sum frequency generation study. Langmuir 20, 357–365.

Yu, S.H., Uan, J.Y., Hsu, T.L., 2012. Effects of concentrations of NaCl and organic acid on generation of hydrogen from magnesium metal scrap. Int. J. Hydrogen Energy 37, 3033–3040.

Zecher, D.C., 1976. Corrosion inhibition by surface-active chelants. Mater. Perform. 15, 33–37.

Zhao, M.C., Liu, M., Song, G., Atrens, A., 2008. Influence of pH and chloride ion concentration on the corrosion of Mg alloy ZE41. Corros. Sci. 50, 3168–3178.

Zucchi, F., Grassi, V., Frignani, A., Monticelli, C., Trabanelli, G., 2006. Electrochemical behavior of magnesium alloy containing rare earth elements. J. Appl. Electrochem. 36, 195–204.

Zucchi, F., Grassi, V., Zanotto, F., 2009. Sodium monocarboxylates as inhibitors of AZ31 alloy corrosion in a synthetic cooling water. Mater. Corros. 60, 199–205.